Large Eddy Simulation for a Deep Surge Cycle in a High Speed Centrifugal Compressor with Vaned Diffuser

Mohamed Alqaradawi

Journal of Turbomachinery

Ibrahim Shahin[1]
Mechanical and Industrial Engineering Department,
College of Engineering,
Qatar University,
Doha 2713, Qatar;
Mechanical Engineering Department,
Shoubra Faculty of Engineering,
Benha University,
Benha, Egypt
e-mails: Ibrahimshahin@qu.edu.qa;
Ibrahim.shahin@feng.bu.edu.eg

Mohamed Gadala
Mechanical Engineering Department,
UBC-University of British Columbia,
Vancouver, BC V6T 1Z4, Canada
e-mail: gadala@mail.ubc.ca

Mohamed Alqaradawi
Mechanical and Industrial Engineering Department,
College of Engineering,
Qatar University,
Doha 2713, Qatar
e-mail: myq@qu.edu.qa

Osama Badr
Mechanical Engineering Department,
The British University in Egypt,
Alshorouk, New Cairo, Egypt
e-mail: osama.badr@Bue.edu.eg

Large Eddy Simulation for a Deep Surge Cycle in a High-Speed Centrifugal Compressor With Vaned Diffuser

This paper presents a computational study for a high-speed centrifugal compressor stage with a design pressure ratio equal to 4, the stage consisting of a splittered unshrouded impeller and a wedged vaned diffuser. The aim of this paper is to investigate numerically the modifications of the flow structure during a surge cycle. The investigations are based on the results of unsteady three-dimensional, compressible flow simulations, using large eddy simulation (LES) model. Instantaneous and mean flow field analyses are presented in the impeller inducer and in the vaned diffuser region through one surge cycle time intervals. The computational data compare favorably with the measured data, from the literature, for the same compressor and operational point. The surge event phases are well detected inside the impeller and diffuser. The time-averaged loading on the impeller main blade is maximum near the trialing edge and near the tip. The amplitude of the unsteady pressure fluctuation is maximum for the flow reversal condition and reaches values up to 70% of the dynamic pressure. The diffuser vane exhibits high-pressure fluctuation from the vane leading edge to 50% of the chord length. High-pressure fluctuation is detected during the forward flow recovery condition as a result of the shock wave that moves toward the diffuser outlet. [DOI: 10.1115/1.4030790]

1 Introduction

The useful operating range of centrifugal compressor is restricted by choke and surge limits. Engineering applications require centrifugal compressor with wide and safe operating range, especially which used in power generation, natural gas industry, and aeropropulsion. Centrifugal compressor surge and stall are an instabilities flow and system phenomenon. During compressor surge, the impeller and casing are subjected to large pressure transients, high loads, high temperature, and, in some cases, causing extensive damage to the entire parts. As a result, compressors operating range extension has been the focus of many existent research studies, which requires new design methods established from understanding of the flow phenomena during surge and the physics of the flow blockage and their prevention or reduction of its effect.

The predictive capability of the numerical solutions based on standard (Reynolds-averaged Navier–Stokes (RANS)) cannot, however, yet be considered as fully accurate predictions of flow details due to the still existing uncertainties and simplification related to inappropriate turbulence modeling, and partly to imperfect accuracy of the numerical algorithms [1]. In fact, turbulent flows in turbomachines are distinguished by a high level of turbulence anisotropy and strong three-dimensionality, which resulting from complex arrangement of bounding walls, tip-leakage flow and other secondary flows, rotational effects, rotor stator interaction (RSI), streamlines curvature, and pressure gradients [2]. The accurate prediction of this complicated flow phenomena has been considered as a significant challenge for the numerical simulation. The time-dependent nature of LES permits the resolution of transient flow structures and can explain the actual mechanisms of vorticity propagation on blade surfaces. It is shown that accurate LES is heavily depending on both the near-wall mesh fidelity and the ability of the imposed inflow condition to recreate the conditions found in the reference experiment [3].

Indeed, from a review of the published studies on using LES turbulence model for computational fluid dynamics (CFD) simulation indicates that centrifugal compressors have received less care than their axial turbo machines counterparts in these countries and especially unsteady aerodynamics flow and surge event. Interference generated in axial turbo machines has received much attention, due to the strict patterns and its wider applications in the aero-engine industry. Tauveron [4] provided correlations and models to describe axial compressor behavior in stall conditions by using LES with two-layer approximate boundary conditions. Tyacke et al. [5] investigated the flow throughout different zones of turbines using LES and hybrid RANS-LES methods and contrasted with RANS modeling. The results show that LES and hybrid RANS-LES produces higher quality data than RANS/unsteady Reynolds averaged Navier–Stokes (URANS) for a wide range of flows. Gourdain [6] investigated the capability of LES to predict the turbulent flow in a stage of an axial compressor. LES successfully predicted the development of high-energy frequencies in the tip region that are uncorrelated to the blade passing frequency, related to the pulsation of the tip-leakage flow. The flow in a centrifugal compressor has been computed using LES for a ported shroud compressor operating near surge [7,8].

Extensive experimental studies have been developed on the unsteady flow in centrifugal compressors focusing on rotating stall and surge phenomena. For a decade, researchers have been working to develop a better understanding of flow pattern in high-speed centrifugal compressors. McKain and Holbrook [9] defined both aerodynamic and manufacturing design details for an advanced 4:1 pressure ratio single-stage National Aeronautics and Space Administration (NASA) CC3 centrifugal compressor.

[1]Corresponding author.

Contributed by the International Gas Turbine Institute (IGTI) of ASME for publication in the Journal of Turbomachinery. Manuscript received September 20, 2014; final manuscript received June 2, 2015; published online June 23, 2015. Editor: Ricardo F. Martinez-Botas.

Table 1 Impeller and diffuser dimensions

Dim.	Impeller
No. of main blades	15
No. of splitter blades	15
Back sweep angle	50 deg
Inlet diameter	210 mm
Outlet diameter R_2	431 mm
Inlet blade height	64 mm
Exit blade height	17 mm
Tip clearance at LE	0.154 mm
Tip clearance at midchord	0.61 mm
Tip clearance at exit	0.203 mm
Dim.	**Vaned diffuser**
No. of diffuser vanes	24
Diffuser vanes leading edge	108% R_2
Diffuser divergence angle	7.8 deg
Diffuser area ratio	2.75
Inlet diameter	431 mm
Outlet diameter	714 mm
Vanes height	17 mm

Table 2 Operating and unsteady simulation parameters

Condition	Value
Design inlet pressure (bar)	1.013
Design pressure ratio	4:1
Inlet temperature (K)	288
Design mass flow rate (lbm/s)	10
Surge mass flow rate (lbm/s)	9.3916
Rotational speed (rpm)	21,789
Total simulated flow time (s)	0.122
Time step (s)	6.6×10^{-6}
Number of time steps	18,485
Number of iteration per time step	10
Hardware operating time per case (day)	90

The surge inception in the NASA CC3 high-speed centrifugal compressor has been studied by many research teams. Spakovszky [10] showed that the unsteady blade-row interaction and coupling is driven by the resonant behavior of the rotor and the stator wave systems. He also stated the existence of backward traveling stall precursors, which was experimentally and numerically confirmed by Skoch et al. [11] and Wernet et al. [12], respectively.

Ni and Fan [13] presented a CFD simulation on the NASA CC3 high-speed centrifugal compressor. A performance map was generated, and the results were compared to experimental findings revealing flow field insights and methods for improving the existing design. Lurie et al. [14] designed a scaled centrifugal compressor stage to be used as a measurement test bed. A CFD-based design process including time accurate calculations of impeller–diffuser interactions was analyzed. The final design is predicted to achieve 1.7% higher total-to-static adiabatic efficiency while simultaneously reducing stage maximum diameter by 23%. Lim et al. [15] presented design and development of the rig to study the surge phenomenon in centrifugal compression systems and to investigate surge control of a compressor using active magnetic bearings servo actuation of the impeller axial tip clearance.

Numerical and experimental investigations on a transonic centrifugal compressor stage with a vaned diffuser are presented by Trébinjac et al. [16]. Unsteady three-dimensional simulations were performed with the Elsa code [16]; they focus on the change in flow structures when the operating point moves from choke to surge. Babak [17] described a surge suppression device utilizing internal recirculation used for stable operating region enhancement of a high-pressure ratio centrifugal compressor. Galindo et al. [18] investigated the effect of pressure pulses' amplitude and frequency on the compressor surge line location. Numerical and experimental investigations on a transonic centrifugal compressor were developed by Bulot et al. [19]. The results were obtained within the impeller, at an operating condition close to the surge of the compressor. Bulot and Trébinjac [20] analyzed the flow structure within the vaned diffuser of a transonic high-pressure centrifugal compressor stage, which operate at the design point. The unsteady flow field analysis was based on a 3D

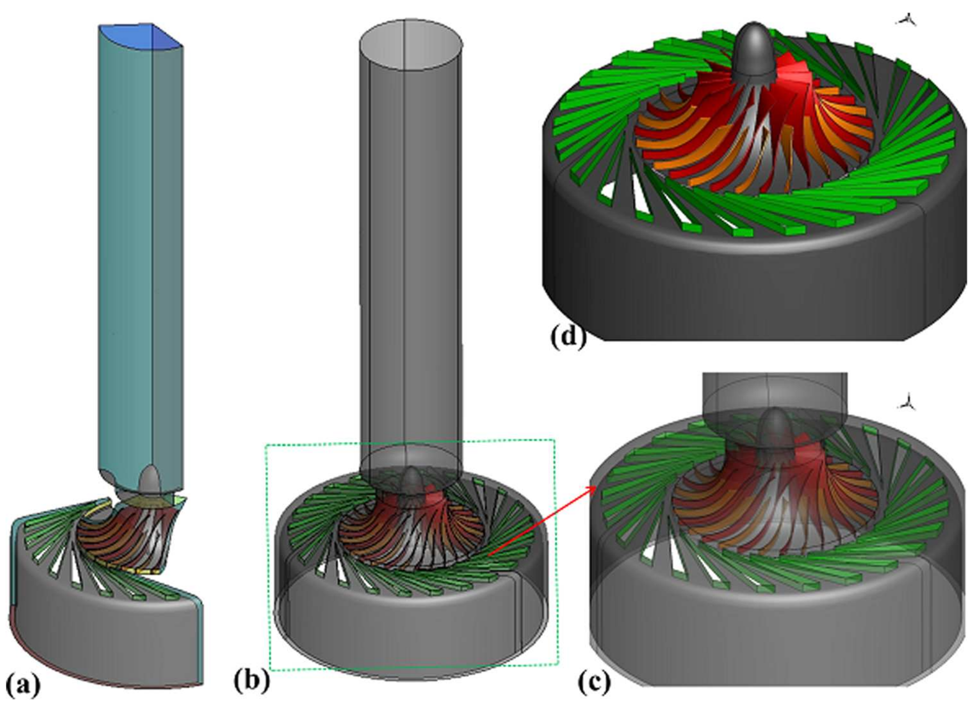

Fig. 1 The geometry of simulated parts: (*a*) 120 deg sector, (*b*) full domain, (*c*) enlarged view, and (*d*) view with casing removal

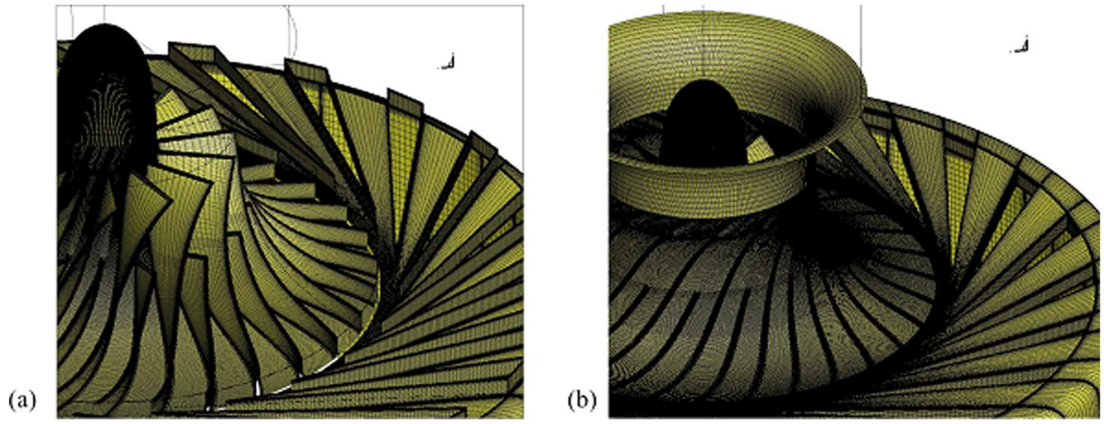

Fig. 2 Computational domain grid: (*a*) with casing removal and (*b*) without casing removal

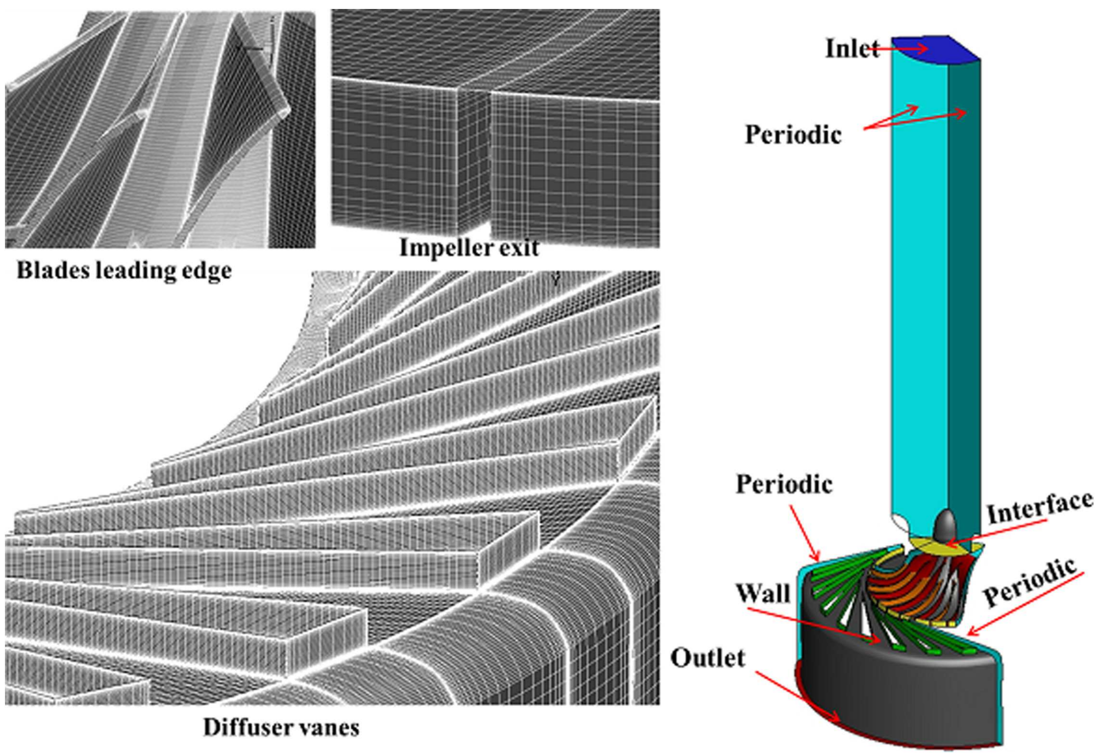

Fig. 3 Mesh details at different locations inside the domain and boundary conditions

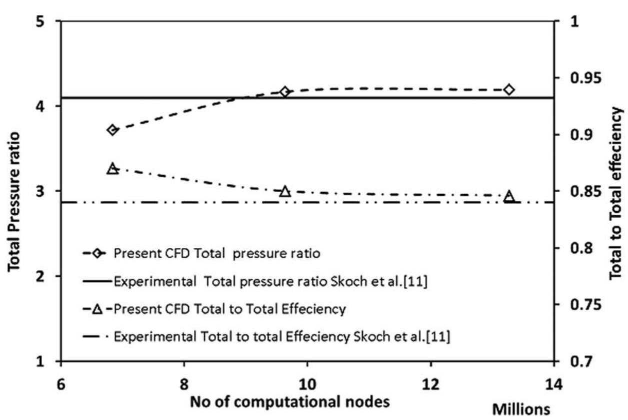

Fig. 4 Performance parameters at design flow rate with different number of computational nodes

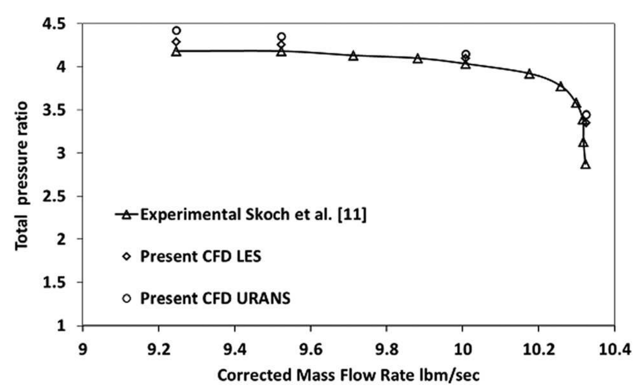

Fig. 5 Pressure ratio of the compressor stage for the present CFD results "URANS and LES models" and experimental results [11]

Table 3 URANS simulation parameters

Condition	Value
Turbulence model	RNG-K-ε
Model constants	$C_{\mathrm{mu}} = 0.09$
	$C_{1-\varepsilon} = 1.44$
	$C_{2-\varepsilon} = 1.92$
Near-wall treatment	Nonequilibrium wall function
Turbulence intensity at inlet	5%
Time step	6.6×10^{-6}
Number of iteration per time step	20

Navier–Stokes code with a phase-lagged technique. Arnulfi et al. [21] conducted numerical simulations and experiments to analysis the industrial compression system behavior under unstable operating conditions and to compare different control devices for surge suppression.

Stein [22] developed a numerical technique for simulating unsteady viscous fluid flow in turbomachinery components. The solver is used to study fluid dynamic phenomena that lead to instabilities in centrifugal compressors. The results indicate that large flow incidence angles, at reduced flow rates, can cause boundary layer separation near the blade leading edge. Ferrara et al. [23] developed experimental tests to investigate the effect of vaneless diffuser type on the stall characteristics; different widths, pinch shapes, and diffusion ratios were tested. The results show that the diffusion ratio has a big effect on the stall pattern and also the stall inception point.

2 Scope of Paper

The main objective of this paper is to investigate the capability of LES to capture the instantaneous flow field and studying the different flow conditions during the initiation of stall and also the compressor deep surge. This paper will give a detailed description of the principal flow pattern found in the impeller inducer and vaned diffuser of a high-speed centrifugal compressor, not only at the presurge condition but also during different time intervals

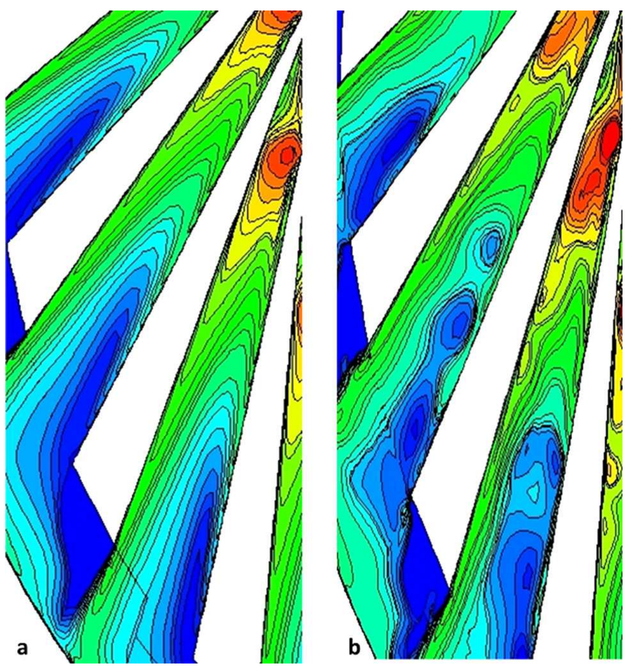

Fig. 6 Comparison of absolute velocities at 95% span plan at off design point: (*a*) URANS and (*b*) LES model

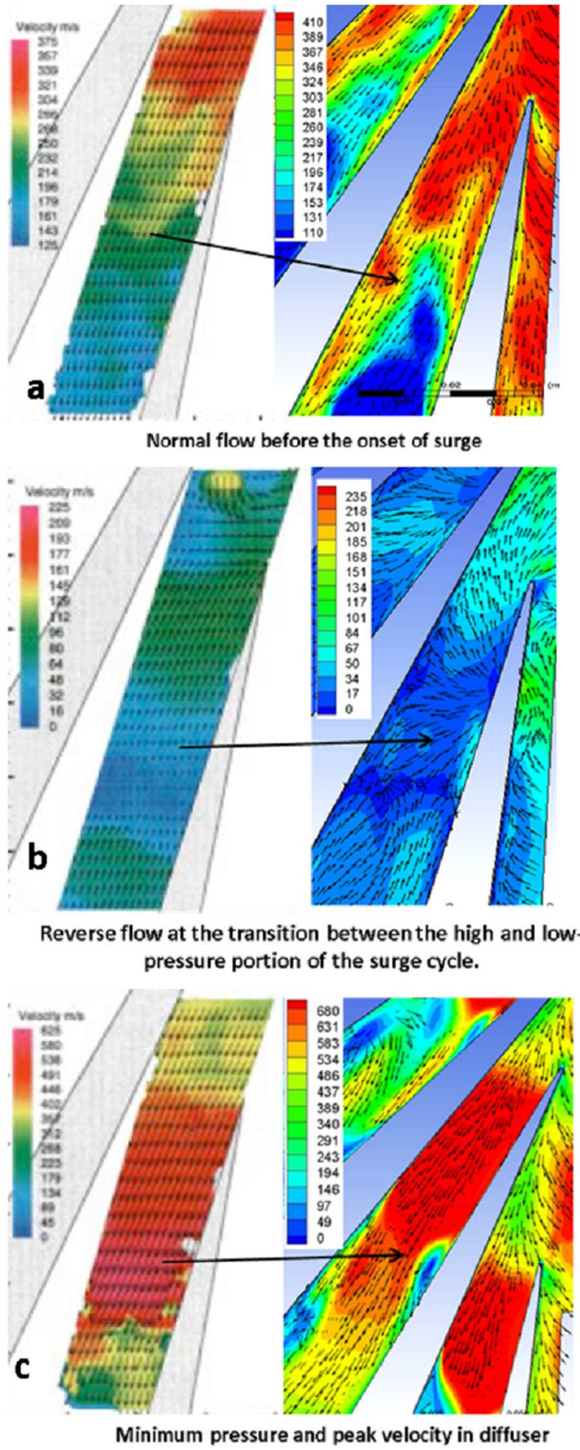

Fig. 7 Comparison of velocities measured [12] "right" and present simulation "left" in the vaned diffuser at different flow conditions during surge

during the surge cycle. Also, the time-averaged and the unsteady pressure loading on the impeller blades and diffuser vanes will presented and discussed during the deep surge phases. The aim is to assess understanding the flow field in a high-speed centrifugal compressor operating at surge and present the techniques that may be used as a stabilization technique to extend the operating range of that type of centrifugal compressor. The flow field data obtained in this work will be used to optimize the location of bleed slots for passive control of rotating stall and surge.

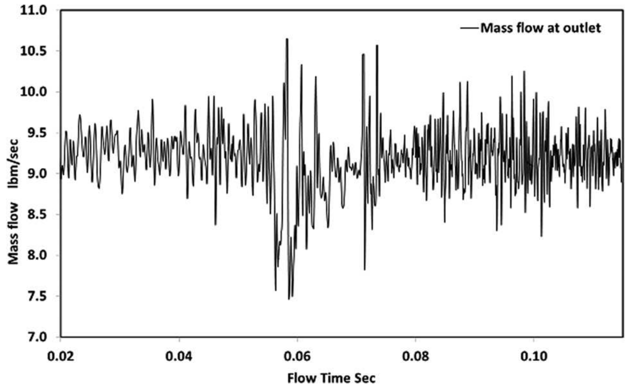

Fig. 8 Area weighted average for the mass flow rate at diffuser outlet

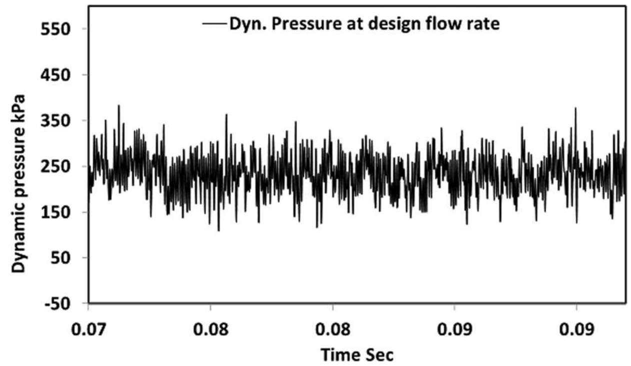

Fig. 10 Dynamic pressure with the flow time at midspan point "1.08R_2" for design flow rate

3 Numerical Procedures

Three-dimensional Navier–Stokes equations [1] are solved for unsteady compressible flow. The sliding mesh is used for simulating impeller rotation, in which multiple cell zones are connected to each other through nonconformal interfaces. As the mesh motion is updated in time, the nonconformal interfaces are likewise updated to reflect the new positions of each zone [24]. The general integral form of the conservation equation formulation for a general scalar, φ, on an arbitrary control volume, V, whose boundary is moving, can be written as follows:

$$\frac{d}{dt}\int_v \rho\emptyset dV + \int_{\partial v} \rho\emptyset(\mathbf{u}-\mathbf{u}_g)\cdot d\mathbf{A} = \int_{\partial v} \vartheta\nabla\emptyset\cdot d\mathbf{A} + \int_v S_\emptyset dV \quad (1)$$

Unsteady large-scale structures and separation zones are the main characteristics of the flow in the centrifugal compressor, so the LES approach is used. In LES, large eddies are resolved directly, whereas small eddies are modeled with the subgrid scale model. A major role of the small scales is to dissipate the turbulent energy that is transferred from the larger scales to the smaller ones through the energy cascade. In the LES approach, the separation between the resolved and unresolved scales is achieved by low-pass spatial filtering of the governing equations. The subgrid-scale stresses resulting from the filtering operation are unknown and require modeling. In the present case, subgrid Smagorinsky–Lilly model is used, in which the eddy viscosity is modeled by the following equation:

$$\mu_t = \rho L_S^2\sqrt{2\bar{S}_{ij}\bar{S}_{ij}} \quad (2)$$

where L_S is the mixing length for subgrid scales, and $\bar{S}_{ij}$ is the rate of strain tensor for the resolved scales. L_S is computed from the following equation:

$$L_s = \min(\kappa d, C_S\Delta) \quad (3)$$

where k is the von Karman constant, d is the distance to the closest wall, C_S is the Smagorinsky constant, and Δ is the local grid scale. In the present case, Δ is computed according to the volume of the computational cell using the following equation:

$$\Delta = V^{1/3} \quad (4)$$

The discretization in space is of second-order accuracy. The interface between moving and stationary parts is set to sliding mesh in which the relative position is updated in each time step. The structured hexahedral mesh is created using ICEM CFD 14.5 blocking tools. The simulation was conducted using high-performance parallel computing on DELL server with four AMD Opteron processor, 48 cores, and 64 GB of RAM, with three-month calculation time for one surge cycle. The CFD code FLUENT with parallel processing, version 14.5 [24], was used to solve the filtered governing equations, which are discretized by the finite volume method. For spatial discretization, a second-order upwind scheme was used. The second-order implicit formulation was

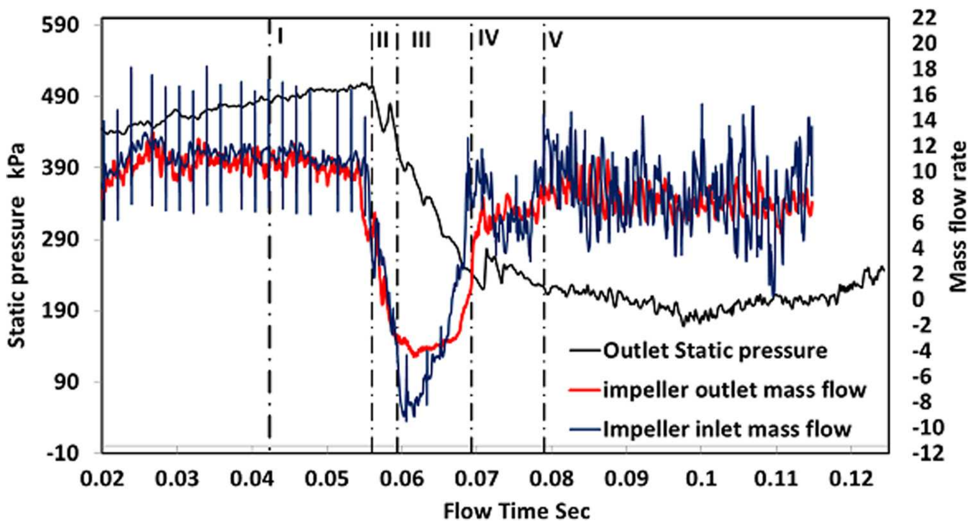

Fig. 9 Area weighted average for the inst. static pressure at diffuser outlet plane and the mass flow rate at impeller with the flow time

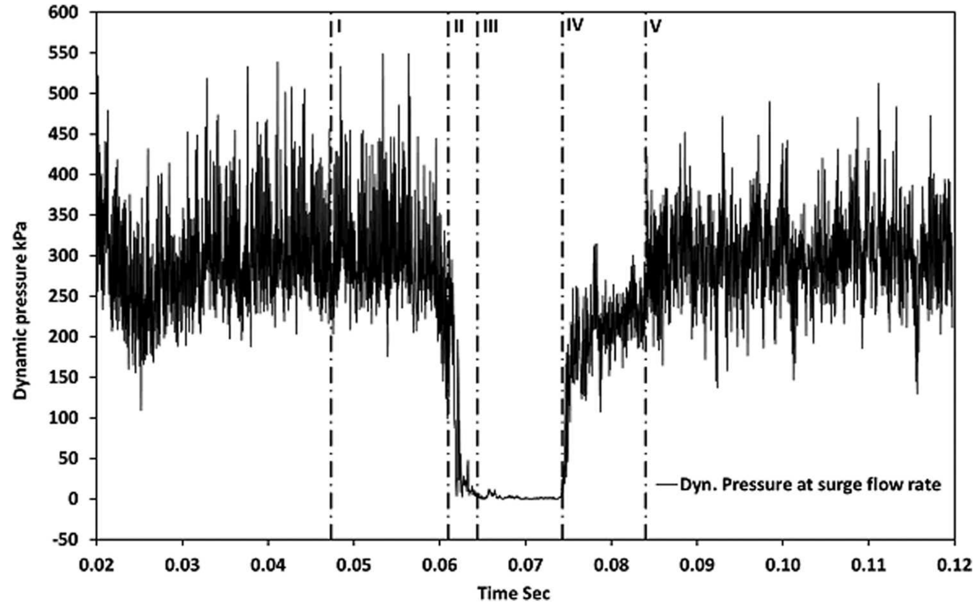

Fig. 11 Dynamic pressure with the flow time at midspan point "1.08R_2" for surge flow rate

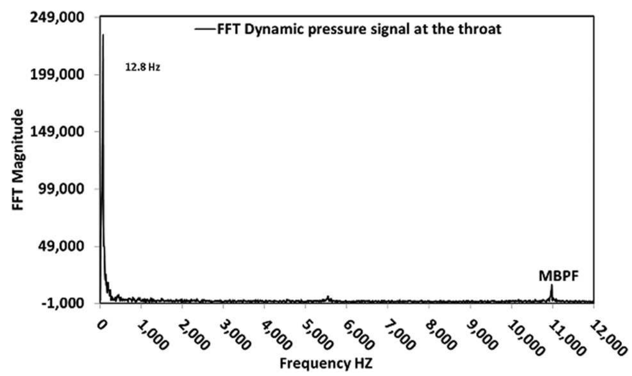

Fig. 12 The FFT analysis for the pressure signal at surge flow rate

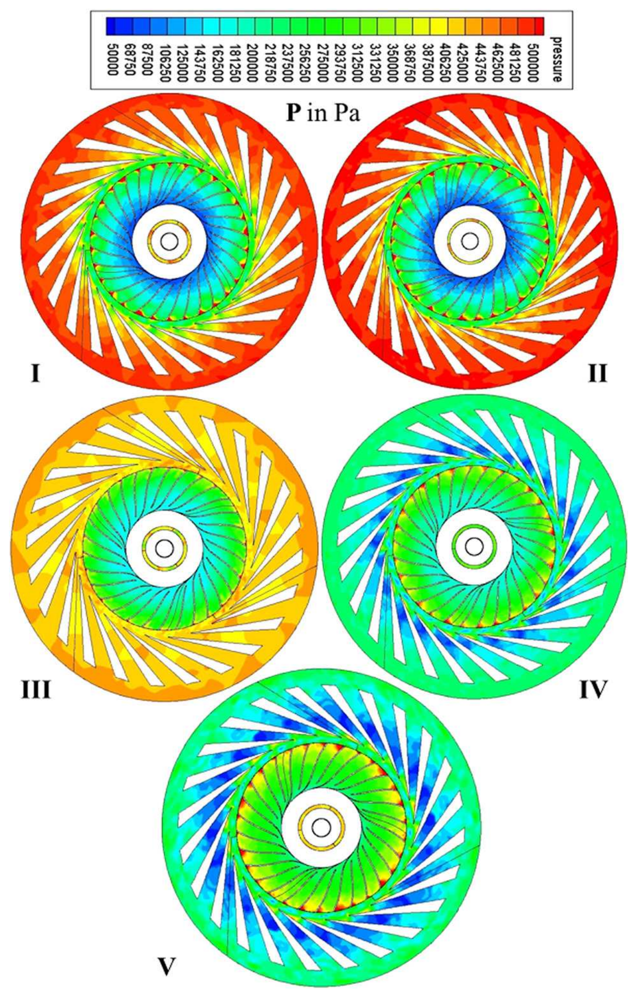

Fig. 13 Instantaneous static pressure in Pa at 95% span plane

used for temporal discretization. In order to resolve the relevant fluctuations, the grid resolution must be high with a small time step, and the Courant number should be smaller than unity to be consistent with the flow properties, which, for this case, gives a time step of 6.6×10^{-6}. Although the sliding mesh is computationally expensive, while handling the rotation of the wheel, the wheel is actually rotating relative to the stationary compressor housing. Also, the blade passage effects are captured and the position of the rotating wheel relative to the diffuser is captured, by which the relevant fluctuations are resolved.

4 Test Case Presentations

The well-studied NASA CC3 compressor was tested over many years at the Small Engine Components Test Facility at NASA Glenn Research Center [10–12,25]. The computational model consists of three parts: the inlet pipe with an inlet bell at its exit, a rotating impeller, and a vaned diffuser with the impeller hub side cavity followed by shaft seal. A straight pipe with a length of 1.5 m is attached at the compressor inlet to insure fully developed flow at the inlet and for a reliable surge prediction. The impeller and diffuser dimensions are shown in Table 1. Also, the operating and unsteady simulation conditions are summarized in Table 2.

The impeller is followed by a wedged vaned diffuser with an annular radial-to-axial bend. The axial bend is extended more than the actual to minimize the effect of outlet boundary conditions on the flow inside the diffuser. Figure 1 shows the basic geometrical simulated domain for the moving and stationary parts. Unsteady simulations of a 120 deg sector "third annulus,"

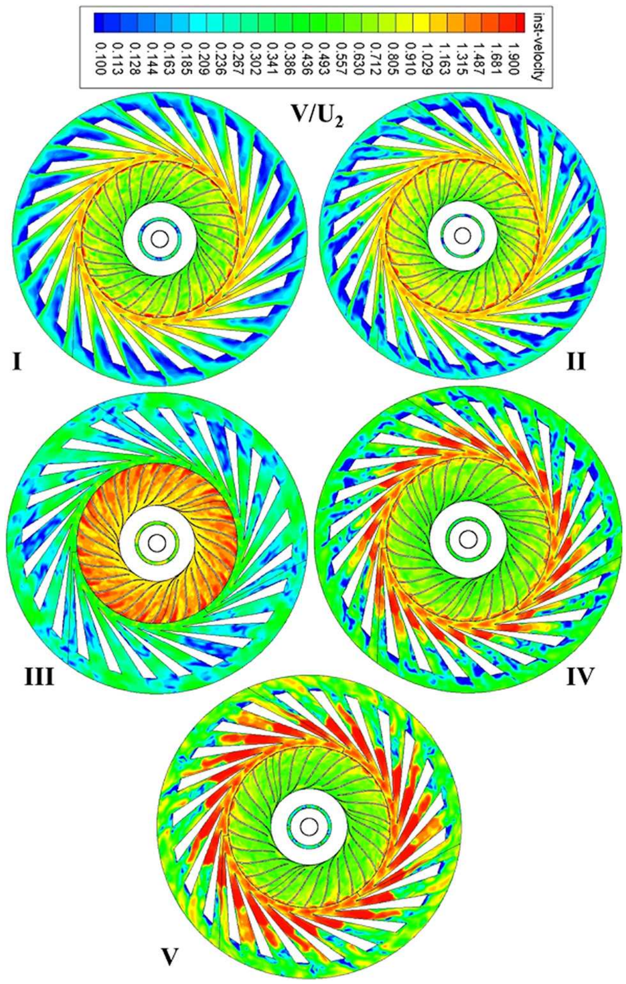

Fig. 14 Dimensionless instantaneous velocity "V/U_2" at 95% span plane

consisting of five impeller main/splitter blade pairs and eight diffuser vanes, used a sliding interface. Although, the full-annulus simulation is recommended in the investigations of stall [26], in order to let the phenomenon develop without forcing any circumferential mode. However, the computational domain may be limited to a periodic sector of the compressor if possible [27]. This compromise allows saving much computational time and use higher number of computational nodes as required for LES, even though it forces the periodicity of the flow. The effect of RSI and of the interactions between rotating stall cells and RSI remains possible with such a computational domain [27,28]; therefore, this assumption is acceptable for the present simulation.

The mass flow inlet boundary condition is used at the inlet of the pipe; the turbulence intensity and hydraulic diameter are also specified. The inlet air was set at atmospheric pressure and temperature equal to 288 K, interface boundary conditions are used at the interface between each rotating and stationary part, pressure outlet boundary conditions are used at the domain outlet, rotating periodic boundary condition is used and wall boundary conditions with no slip velocity are employed on walls. Multiblock structured hexahedral mesh with 9,629,414 cells is used for the simulated 120 deg sector, as shown in Fig. 2. In order to capture the boundary layer, which is very important for compressor flows, the mesh is refined at the walls. The blade tip clearance is resolved with ten cells in the radial direction. The first grid point from the wall is located to capture near-wall effects, with distance to the first grid point from the wall set such that the viscous wall distance ($y+$) is near 1. The boundary conditions used are shown in Fig. 3. The data monitor and convergence criterion "1×10^{-4}" are used to judge the computation convergence for the unsteady calculations. The mass flow at duct inlet, impeller inlet, impeller outlet, and diffuser outlet are monitored during the calculations; also the static and dynamic pressure are monitored at different locations in the simulation domain such as impeller inlet, impeller outlet, diffuser outlet, and diffuser throat.

5 Mesh Sensitivity Study and Numerical Model Validation

In order to ensure the accuracy of present numerical solution, a careful check for grid independence was conducted. Three numbers of computational nodes were used 6.83, 9.63, and 13.27 million of nodes. The numbers of nodes are changed by increasing the number of elements for the impeller and diffuser in meridional, radial and spanwise directions. Performance parameters at design flow rate with different number of computational nodes are shown in Fig. 4, for Skoch et al. [11] experimental results and present CFD. The present results with 9.63 million of nodes agree well with experimental data from Ref. [11], and no noticed change is resulted by increasing the nodes to 13.27 million of nodes. So the grid with 9.63 million of nodes was used for all the studies conducted in the present simulation.

In this section, the computed data are compared with measured data to validate the developed model. The total pressure ratio of the stage is shown in Fig. 5 for the present CFD simulation based on URANS and LES and compared with experimental results of Skoch et al. [11]. The URANS parameters are shown in Table 3. The corrected mass flow is defined in the following equation:

$$\dot{m}_{\mathrm{cor}} = \frac{\dot{m}\sqrt{T_{01}/T_{\mathrm{ref}}}}{p_{01}/p_{\mathrm{ref}}} \tag{5}$$

The trend of the experimental results is well predicted by the URANS approach, but the pressure ratio is overestimated at off-design operating point especially near the stall limit. At design operating conditions, URANS slightly overestimated the pressure ratio while the results based on LES have a good agreement with the experimental results at the design operating point and at lower flow rates. To indicate the reasons for these differences with measurements, the instantaneous velocity at 0.95 span plan of the diffuser is compared for URANS and LES in Fig. 6. The influence of separated flow in diffuser channels is predicted well by LES more than that predicted by URANS. The size of the low-momentum region is also larger in the case of LES than with URANS. LES field shows higher predicted losses in the diffuser part more than that predicted by URANS, and this explain the overestimated total pressure ratio by URANS.

In order to validating unsteady flow variations, the instantaneous velocity contours at 95% span plan of the diffuser throat are shown in Fig. 7. The present CFD results were compared to measurements [12] at different instant times during surge cycle. Figure 7(*a*) represents the normal flow conditions just before the surge onset, the presents CFD predicted the distribution correctly comparing with measurements as the maximum velocity is 375 m/s at the minimum area and the velocity decreases gradually toward diffuser exit to the range between 125 m/s and 150 m/s. The reverse flow phase of the surge cycle is shown in Fig. 7(*b*), the numerical results predicted a back flow appearance with a maximum velocity value around 110 m/s at the diffuser throat, and this result is close to the experimental result of 112 m/s. The peak velocity in the diffuser condition which corresponding to the minimum pressure is also well predicted as shown in Fig. 7(*c*), there is a small region with a corrected flow direction appears at the diffuser throat, while the numerical results proves the same result but with slightly higher velocity magnitudes. It may be concluded from Fig. 7 that the present CFD model with LES can capture the complicated unsteady flow variations during surge accurately.

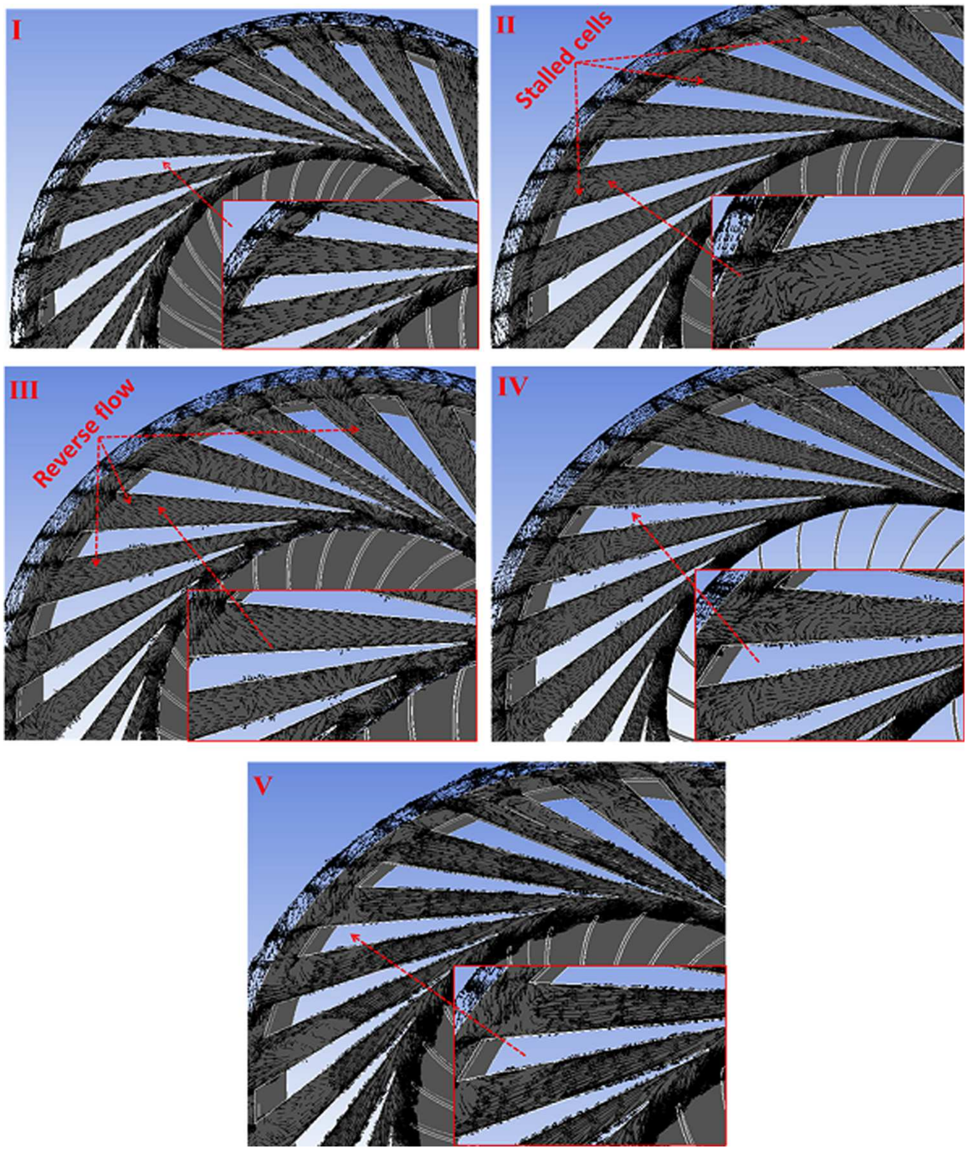

Fig. 15 Instantaneous velocity in the diffuser

6 Unsteady Flow Analyses During Surge Cycle

6.1 Surge Cycle Characteristics. The unsteady flow pattern for the surge condition is investigated by recording the area weighted average static pressure and mass flow signals with the flow time at different locations. All these signals are acquired as operating flow rate is reduced just after the surge flow rate 4.26 kg/s mass flow and 21,789 rpm. Figure 8 presents the time-resolved mass flow rate at diffuser exit, the fluctuation in the outlet mass flow is noticeably higher amplitude fluctuations were observed, these amplitudes reach the maximum value during the time at which the backflow occurred.

The instantaneous static pressure at the diffuser outlet is also presented in Fig. 9. When the mass flow decreases under the surge limit, the model predicts well the deep surge development. The instantaneous static pressure increases in the diffuser until the impeller can no longer work against the developed head. The high-pressure fluid in the diffuser forces the flow to move back into the vaneless part, casing a sharp pressure failure in the vaned diffuser. Impeller flow during surge is characterized by even larger mass flow oscillations, which becomes negative for part of the cycle; see Fig. 9. In reversed flow, the instantaneous operating point moves down a line known as the negative flow characteristic. The surge event also characterized not only by high mass flow fluctuation at impeller inlet but also the flow reversal at the front of the impeller is detected. The initiation of surge event is defined as the point at which the amplitude of the pressure trace starts to grow and a distinct oscillation frequency appears and reaches a maximum value of 510 kPa as measured by Wernet et al. [12], which are pointed out in Fig. 9. The dynamic pressure signal at midspan point "$1.08R_2$" is shown in Figs. 10 and 11 for design and surge flow rates, respectively. High-pressure fluctuations are observed in the data, which indicate the compressor surge event. The stable operating point pressure was about 360 kPa, while during the surge a peak pressure of 550 kPa and low dynamic pressure value reached 0 Pa. The corresponding sharp decrease in dynamic pressure occurs at the same time that the static pressure reaches maximum value. The flow is reversed in the diffuser at that time and becomes stagnant for 0.01 s; then the dynamic pressure increases as the flow starts to recover and goes in the forward direction.

6.2 Spectral Analysis for Dynamic Pressure. The unsteady variations in dynamic pressure are noted down at midspan point, one after the impeller exit "$r = 1.8R_2$"; this location is used

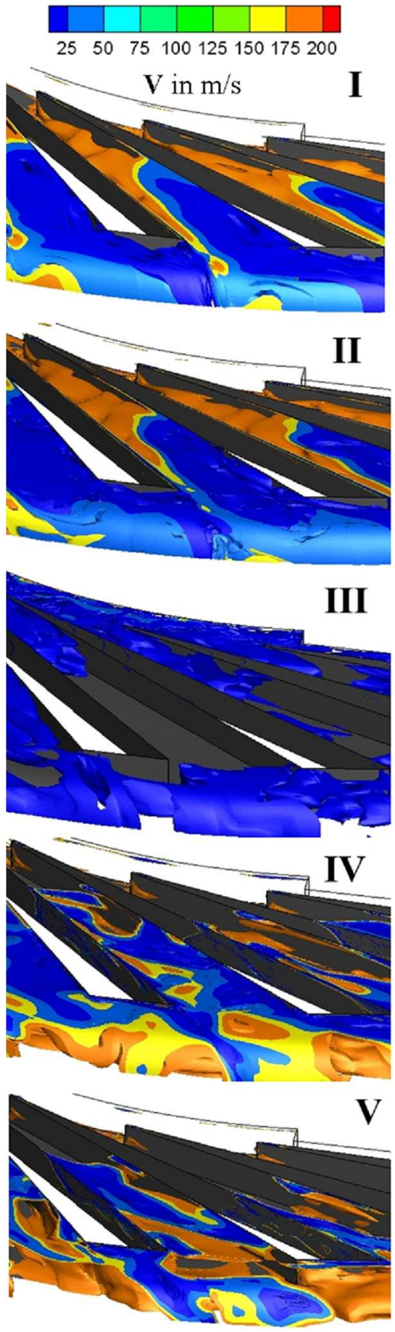

Fig. 16 Isosurface for instantaneous velocity in the diffuser

because the pressure signal obtained at this location is not dominated by blade loading but is still close enough behind the impeller exit that the jet-wake pattern still persists. The pressure signal from the time domain is converted into the frequency domain by fast Fourier transformation (FFT) in order to understand the intensity of interaction in the flow field. Figure 12 shows the FFT analysis for the pressure signal at surge flow rate; the surge frequency becomes dominant, and the frequency content is not only limited to the blade passing frequency. The increasing of the magnitude is caused by the glowing oscillation of the main flow along the compression system, which is at a very low frequency.

6.3 Vaned Diffuser Instantaneous Flow. In this section, the instantaneous flow results are presented and discussed. The results are analyzed at time intervals during a surge cycle I, II, III, IV, and V, which are indicated in Figs. 9 and 11. The unsteady static pressure and absolute velocity at 95% span plane through the impeller and vaned diffuser are shown in Figs. 13 and 14.

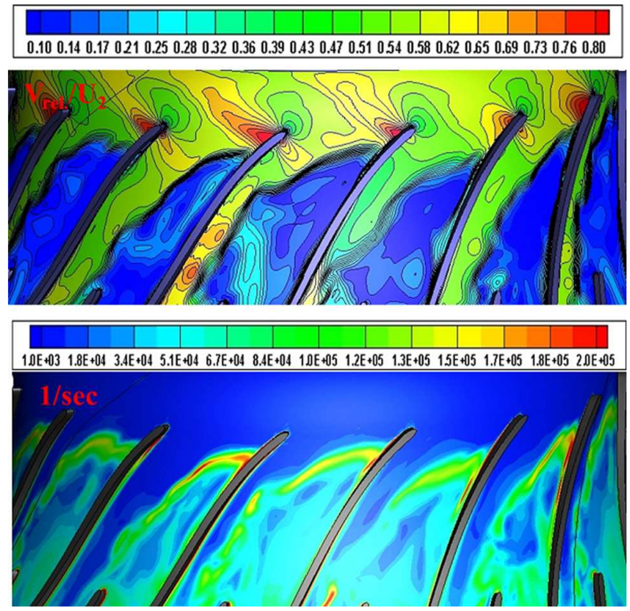

Fig. 17 Vorticity magnitude and relative velocity prior to surge

(I) *Presurge interval:* This phase starts when decreasing the mass flow to the surge flow, which causes an increase in back pressure and the flow, separated on the diffuser vane walls. As shown in Fig. 13, rotating instabilities in the passage is observed toward the diffuser exit. Also, there is a larger area with low-momentum fluid on the suction side of the diffuser channels. The low-momentum fluid on diffuser channels causes a reduction in the effective flow area.

(II) *Surge inception:* This phase starts due to the large rise in the static pressure in the diffuser channels. The rotating instabilities are one of the main characteristics of this phase. A number of stall cells are observed near the diffuser van trailing edge. The fluctuation of mass flow rate and the pressure causes an increase of the rotating stall cells size and consequently, a larger blockage in the diffuser channels is developed. The impeller develops pressure to move the fluid against the blockage in the diffuser, which will lead to start of the surge event. Figures 13–16 depict the evolution of the flow feature in the diffuser during surge intervals. The large change in static pressure at the diffuser throat is observed with time, which indicates the compressor surge event. The static pressure at the diffuser throat increases from 360 kPa at stable operating point to a high oscillating pressure with peaks of 500 kPa. At some part of the diffuser vane passage, a stall zone appears toward the pressure side; it builds up and then dies down. Weak recirculation is detected in some passages close to the vane pressure surface (PS). In contrast, a much stronger recirculation of the same sense is detected in other passages, and closer to the center and suction side, which is also observed by Wernet et al. [12].

(III) *Flow reversal interval:* The low-momentum fluid and stalled zones in the diffuser causes a decrease for flow area of the diffuser, which results in an increase of the pressure until the impeller developed pressure cannot longer overcome the adverse pressure from the diffuser passages. The higher pressure fluid in the vaned diffuser area is moved backward into the impeller exit, resulting in a pressure failure in the diffuser. A back flow through the diffuser channels was observed during this interval

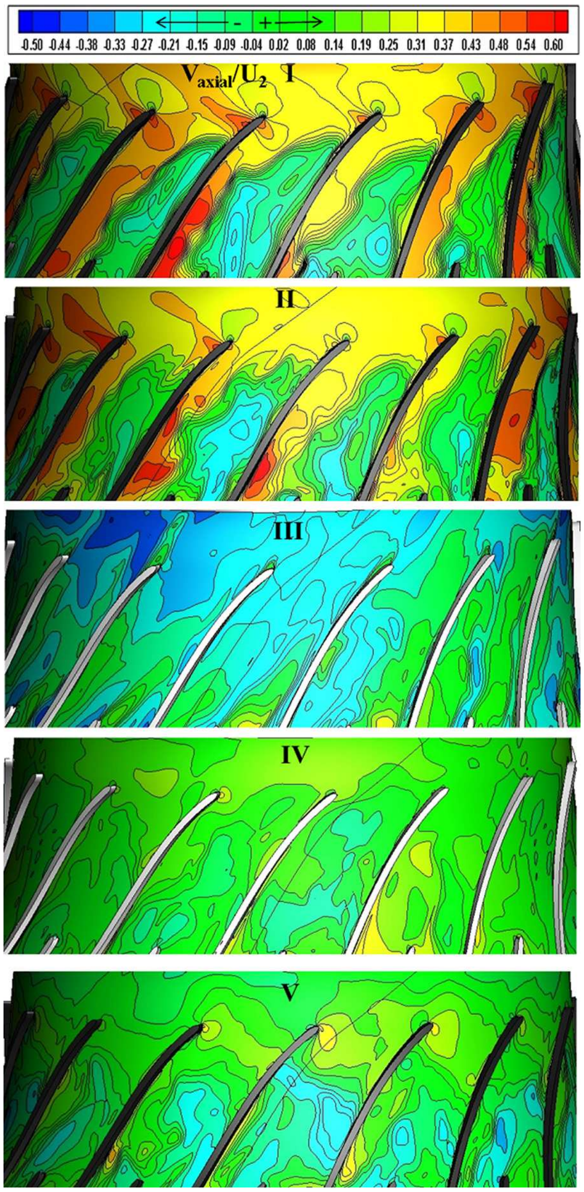

Fig. 18 Dimensionless instantaneous axial velocity "V_{axial}/U_2" at 95% span plane

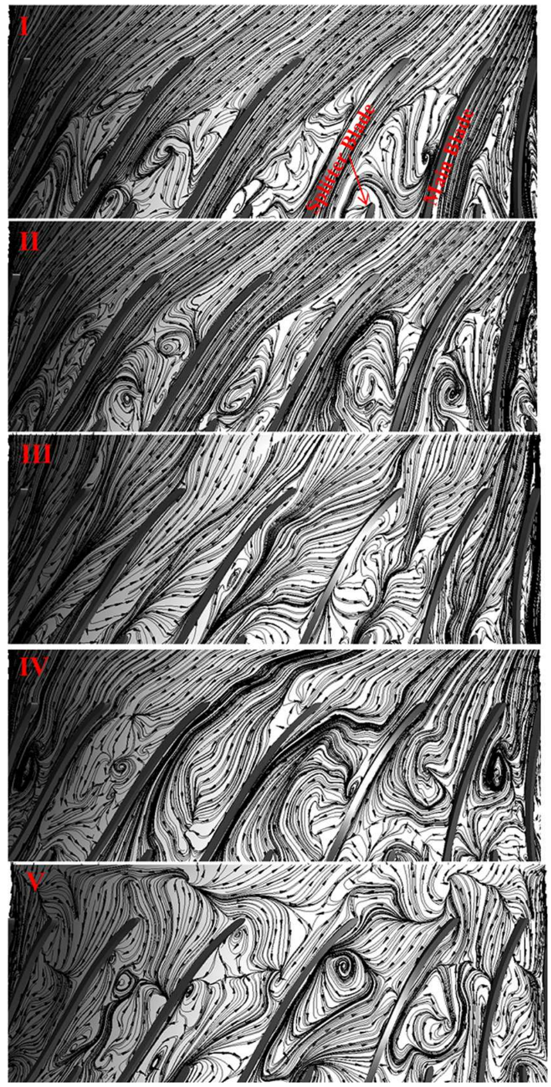

Fig. 19 Streamlines and velocity vectors in impeller inducer "95% span plane" at different surge phases

Fig. 15; the start of the flow reversal condition is characterized by an increase in the diffuser throat pressure. The vaneless area pressure increased due to the sudden collapse in diffusion is taking place upstream of the diffuser throat [12]. The reversed flow interval is also characterized by compression wave upstream into the vaneless space. The relative position between the impeller blades and the diffuser vane effects on the characteristic of the reversing flow. During backflow, some passages of the diffuser have a completely reversed flow, whereas others have a flow reversal in some parts. In the absence of the impeller blade and due to pressure difference between the diffuser exit and the diffuser throat, a backflow in the diffuser vane channel is occurred, with highest value of velocity at throat area. As pressure gradient through the diffuser passage is depend on where we are in the surge cycle; so, the magnitude of the reversing flow is highly depends on pressure gradient in the diffuser [12]. The reversed flow depends not only on the flow time but also spatial variations are observed for the reversed flow. The reversed flow fluid in the diffuser also contains streamwise velocity variation.

(IV) *Recovery flow inception:* This phase starts at time interval IV, when the flow reattaches back to the normal direction. The pressure difference causing the backflow is lower than that observed in the case of the flow reversal as shown in Fig. 13. At this condition, the pressure difference that causing the reverse flow has become in equilibrium with the impeller outlet pressure, which results in a forward recovered flow in the diffuser channel. Figure 13-IV shows the surge cycle static pressure that illustrates the flow recovery start, which re-establishes the normal flow direction and pressure recovery through the diffuser [12]. Figure 14-IV shows the velocity field at a condition just prior to the minimum pressure in the diffuser region. The failure in pressure causes a move of air to flow to the diffuser and the static pressure and mass flow rate increase. As shown by the velocity vector, the flow from the vaneless area into the diffuser channels become similar to a flow through convergent/divergent nozzle, and a supersonic flow is developed just after the throat with velocities on the order of $1.48U_2$. Stagnant flow is observed in front of the supersonic wave. This stagnated region is the reversed flow residue as shown in Fig. 14-III,

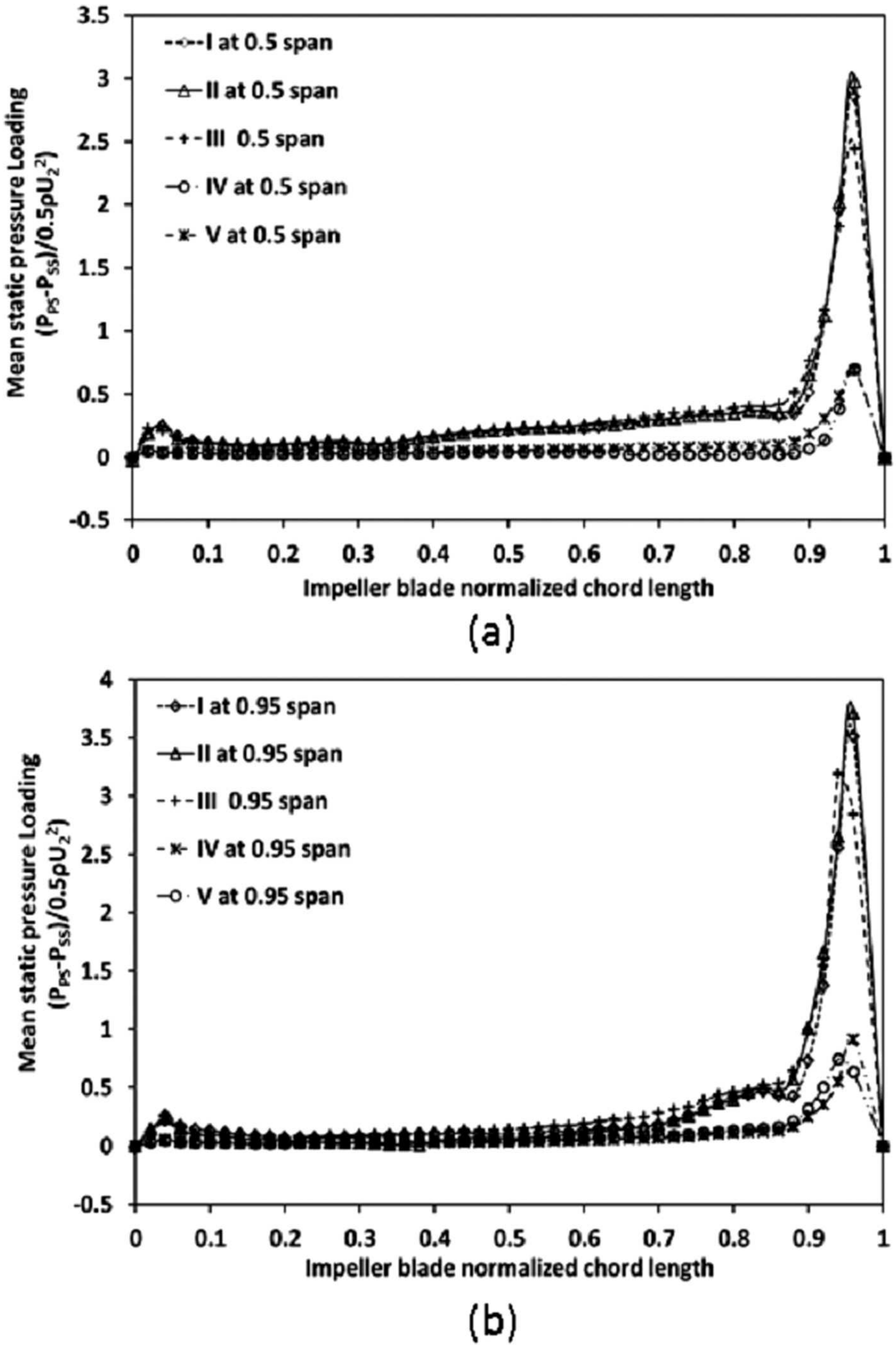

Fig. 20 Impeller blade mean static pressure loading at: (*a*) 50% span and (*b*) 95% span

which occurs at the flow reversal phase of the surge cycle.

(V) *Repressurization phase:* Fig. 14-V shows the continuation of the flow recovery which characterized by the highest flow velocity in the diffuser. The maximum velocity detected at this phase was $1.68U_2$. The relatively uniform flow outside the diffuser steadily accelerates as it enters the diffuser throat. The propagation of the shock front is readily observed just above the low-velocity flow region. The pressure then slowly recovers from the minimum value back to the stable operating point pressure level before the next surge cycle begins.

Figure 16 shows the isosurface for instantaneous velocity in the diffuser range 20 to 200 m/s. Different time intervals during the surge cycle are indicated. Prior to the initiation of the surge event, a corner separated flow is developed near the hub corner just after the vane leading edge. The low-momentum fluid through the diffuser is also shown in Fig. 16, for all surge cycle phases.

6.4 Impeller Inducer Flow. Unsteady numerical results at the impeller inducer and near the shroud are now presented, as the origin of the destabilization occurs generally in this specific location. The vorticity magnitude and relative velocity contours near tip clearance at 95% span are shown in Fig. 17 for surge flow rate and time "I." The operation at surge flow leads to a gradual decrease of the mean flow velocity, which causes the incidence angle on the impeller main blades to rise. The high incidence at low mass flow rate and adverse pressure gradient in the impeller causes the boundary layer to thicken and separate on the impeller main blade suction side. The tip-leakage flow enters the passage

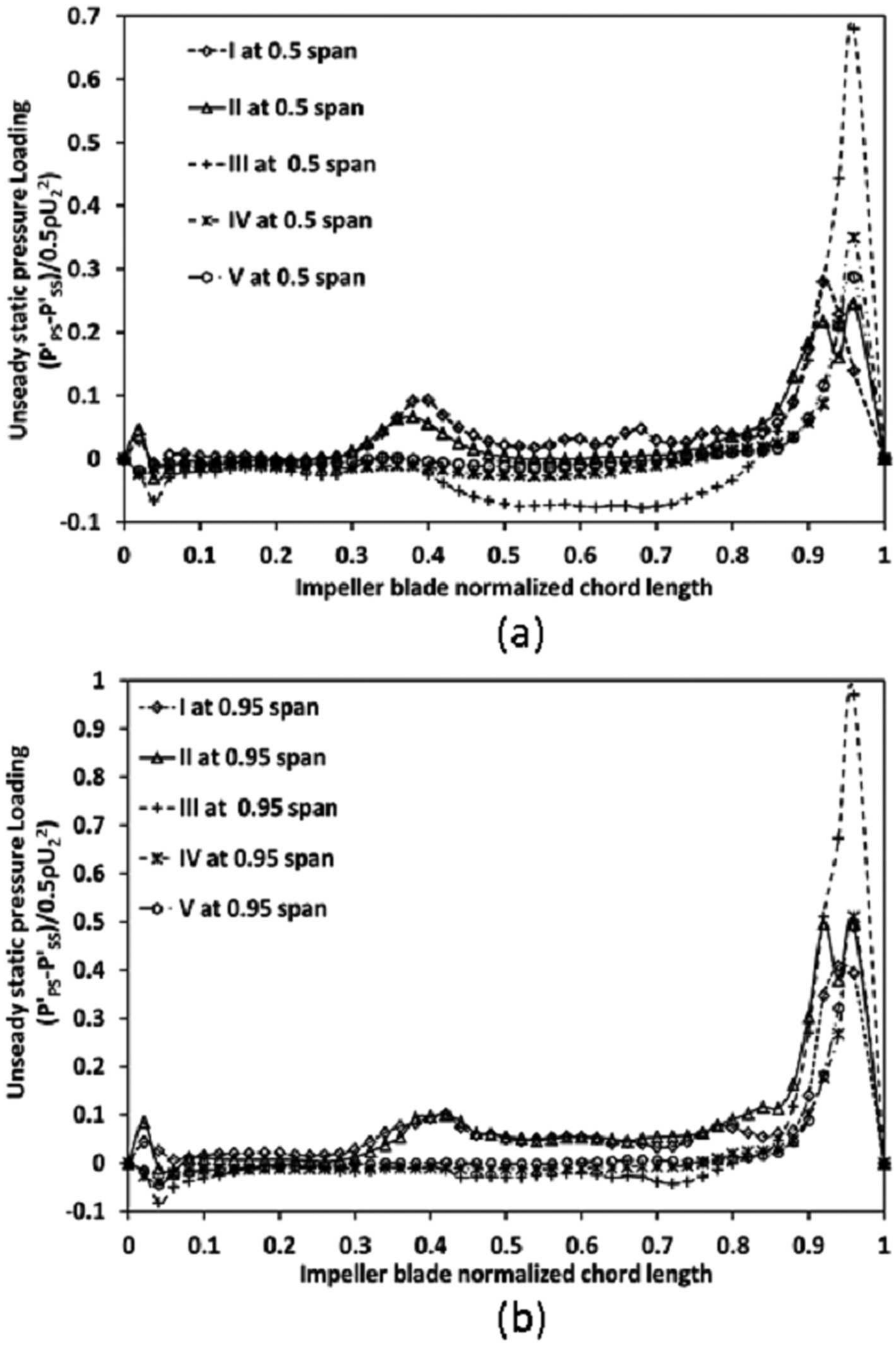

Fig. 21 Impeller blade RMS static pressure loading at: (*a*) 50% span and (*b*) 95% span

upright to the blade suction side. The impeller inlet flow converges with the tip-leakage flow and deflects it. Because the incoming flow, which has a high incidence angle, and the tip-leakage flow are at different flow angles, a discontinuity in fluid properties exists. This discontinuity in fluid properties rolls up into the core of the tip-leakage vortex.

The relative velocity normalized by the impeller tip speed near the shroud indicates the interactions of the tip leakage with the main flow; which causes an interface surface between the low-momentum fluid and the high-momentum fluid. The interaction surface extends from the main blade suction and reaches the pressure side of the adjacent main blade. The low-momentum fluid near the main blade suction side is then stretched and transported by the leakage flow of the main blade in the middle of the channel (Fig. 17). As a result, the wake region significantly enlarges.

The evolution of axial velocity and the velocity vectors at 95% span of the impeller inducer for different time intervals are presented in Figs. 18 and 19, respectively. At flow time I, the axial speed is positive at the impeller inlet. However, a negative axial speed zones are detected at the main blade suction side. Also, high positive axial speed region is observed near the pressure side of the main blade. The inducer area with negative axial velocity is consider as the region the tip-leakage flow is fed into, the region of the tip-leakage vortex is bounded by positive and negative axial velocity areas. The main blade tip clearance flow and the boundary layer of the main blade suction side hits the splitter pressure side. A part of this flow moves upstream, creating a reverse flow zone.

At flow time II, the zone with negative axial speed has extended toward the blade leading edge, inducing large zones of negative

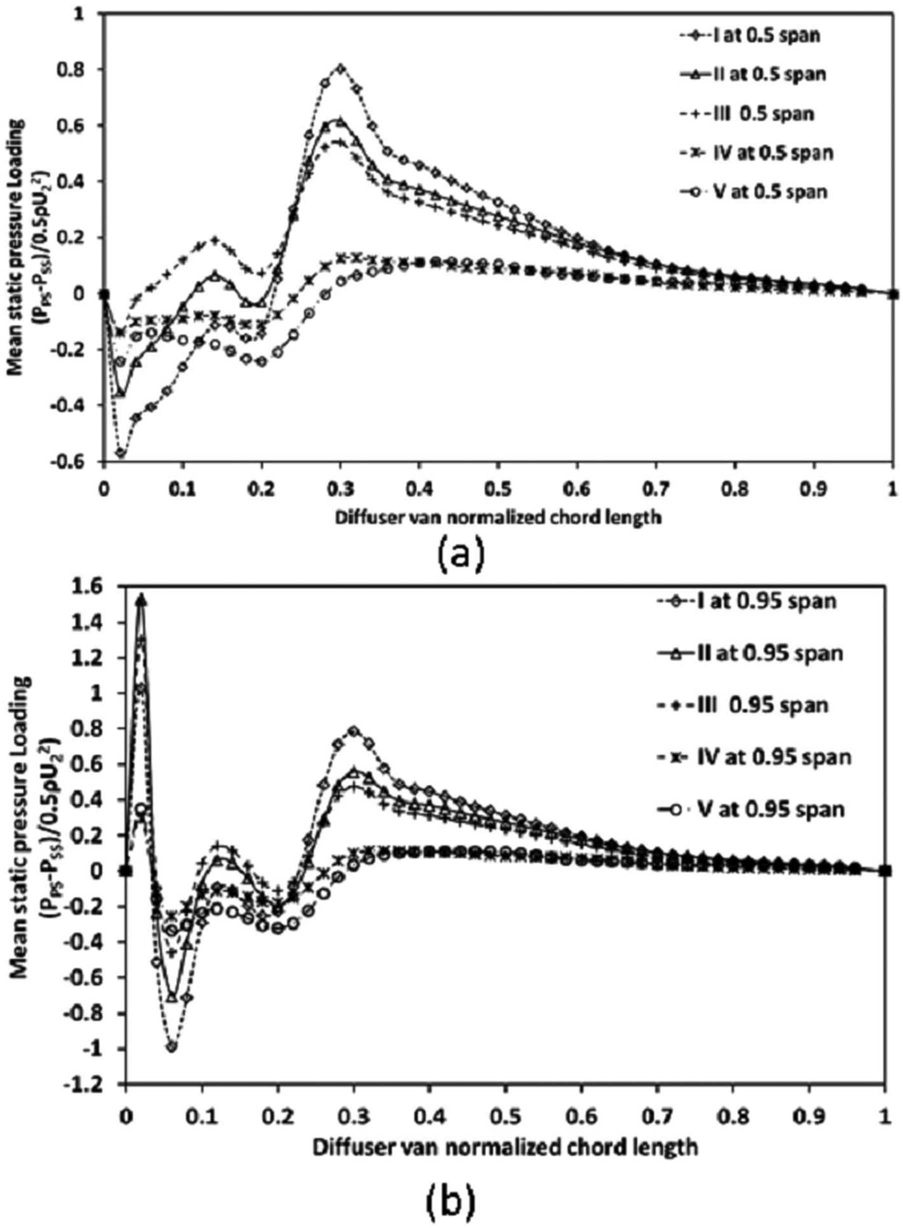

Fig. 22 Diffuser vane mean static pressure loading at: (*a*) 50% span and (*b*) 95% span

axial speed in the impeller passage. The tip leakage over the blade tip has a tendency to flow back toward the impeller inlet owing to the negative pressure gradient. The backflow will interact with the incoming main flow, which has a high incidence angle. This interaction of the tip leakage with the main flow is the main reason for the onset of compressor stall. At flow time III, the flow reversal reaches the front of the impeller. This flow reversal has its origin from the diffuser region. Distinct backflow is located at or near shroud section. A second compelling indication of flow reversal through the impeller was indicated by drawing the velocity vectors inside the impeller as shown. The axial velocity contours shown in Fig. 18-III indicate that the flow reversing in the diffuser not only propagates into the vaneless space but also flows all the way out through the front of the impeller. Figures 19-IV and 19-V show the flow recovery condition in the impeller inducer.

6.5 Impeller Blade Pressure Loading. Figure 20 shows the time-averaged loading on the impeller main blade at two spanwise locations. The x axis represents the impeller blade normalized chord length, where "0" corresponds to the leading edge of the main blade and "1" corresponds to the trailing edge. The y axis represents the time-averaged loading, which can be defined as the difference between the static pressure on the PS, "P_{PS}," and the static pressure on the suction surface (SS), "P_{SS}." The blade loading is normalized by the dynamic pressure head based on the density at the impeller inlet and the impeller tip speed. For times I, II, and III, a gradual increase in loading is noticed from 35% of the chord length loading, but a large variation in the mean loading values is observed from 85% of the impeller chord length with the highest value at 95% for time II. For the flow recovery conditions "IV and V," the axial inducer section is barely loaded. The unloading in the inducer section is consistent with the inlet tip recirculation postulated earlier for low-mass-flow conditions. At 95% span, the same behavior is obtained but with higher loading values especially near the blade trailing edge. In conditions I, II, and III, a locally high loading is seen at the main blade leading edge. This locally high loading at the leading edge is caused by positive incidence at part load.

To visualize the unsteady pressure distribution on the blade surface, the difference in pressure fluctuation between the pressure

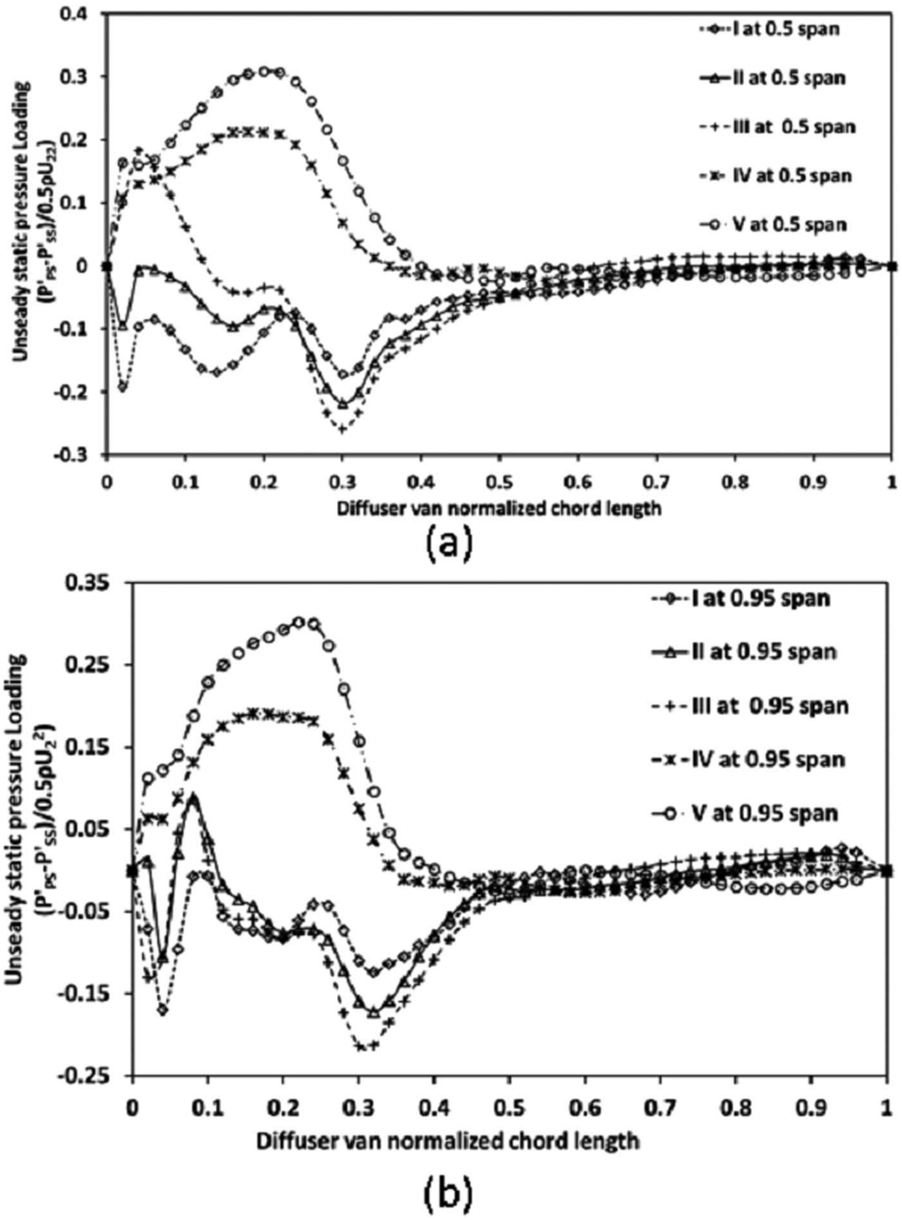

Fig. 23 Diffuser vane RMS static pressure loading at: (*a*) 50% span and (*b*) 95% span

and suction sides is plotted and normalized by the dynamic pressure head based on the density at the impeller inlet and the impeller tip speed. Figure 21 shows the unsteady pressure loading from leading to trailing edge at midspan and near tip. There is no noticed blade forcing in the inducer region, but a small loading is seen at 30% of the blade chord length and a higher unsteady loading is seen for the rear part of the blade. At the blade trailing edge, the amplitude of the unsteady pressure fluctuation is maximum for time III and reaches values up to 70% of the dynamic pressure for the flow reversal condition. The maximum unsteady blade loading was found at 95% to 100% of the streamwise location near the tip.

6.6 Diffuser Vane Pressure Loading. Figure 22 shows the time-averaged variation of diffuser vane loading at two spanwise locations 50% and 95%. The vane loading plot reveals that till a streamwise location of 0.2 there is negative loading followed by positive loading with a maximum value at 30% of the vane length; a variation in the vane loading with time is also noticed. The variations are getting stronger at 30% of the vane length. The unloading of the diffuser vane is observed toward the trailing edge from a streamwise location of 0.8. Unloading occurs when the pressure difference between the vane PS and the vane SS gradually comes to zero. The diffuser vane loading also exhibits higher values at 0.95 spans, without any variation for the location at which the unloading occurs.

Figure 23 shows fluctuating blade loading distributions on diffuser vane at midspan and near the shroud. The diffuser vane exhibits high-pressure fluctuation from the vane leading edge to 50% of the chord length. Unloading is observed from 50% of chord length toward the trailing edge. High-pressure fluctuation is detected during the forward flow recovery condition with maximum values at 20% of the vane length. The reason is that there is a shock front that propagates back down through the diffuser.

7 Conclusions

A deep surge cycle has been successfully simulated for a high-speed centrifugal compressor. The simulation performed with LES as a turbulence model to capture the unsteady large-scale structures and separation zones during the surge event. The results through the LES are compared qualitatively and quantitatively with experimental results of Wernet et al. [12]. The static and dynamic pressure data with the flow time during surge are presented and discussed. Also, the impeller flow rate and flow direction are monitored with the flow time and used to specify the surge phases. The mean and unsteady pressure loading during surge phases were captured on the impeller blades and diffuser vanes surface. The main results obtained and the phenomena described in this paper can be summarized as follows:

(1) The aerodynamic phenomena that happen during the deep surge were captured accurately with LES CFD simulation. This study also confirms that LES better predicts performance and the unsteady flow features in centrifugal compressors than URANS, especially at lower mass flow rates.
(2) The dynamic pressure signal monitored at the diffuser throat described well the deep surge event. The dynamic pressure exhibit high-fluctuation followed by a sharp drop values near zero and then a sudden increase in pressure indicating flow reattachment again.
(3) The unsteady flow during the surge phases has been identified through the diffuser and impeller inducer parts. During the surge inception, a vortex tube is generated a long the diffuser vane pressure side. The rotating instability flow patterns are different for each diffuser channel, resulting from the relative position between the impeller blades and diffuser vanes.
(4) During the reversed flow condition, a nonperiodic reversed flow pattern was detected not only on the diffuser channels but also through the impeller inducer blade channels.
(5) During the flow recovery condition, Small stalled cells were observed in front of the shock wave till the flow completely recovered.
(6) The impeller blades and diffuser vanes loading during the deep surge phases are also identified. The time-averaged loading on the impeller main blade is maximum near the trialing edge with higher values near the tip, while the unsteady loading is maximum for the flow reversal condition and reaches values up to 70% of the dynamic pressure. The diffuser vane exhibits high-pressure fluctuation from the vane leading edge to 50% of the chord length, which results from the shock front during the flow recovery phase.

Acknowledgment

This publication was made possible by NPRP Grant No. 4-651-2-242 from the Qatar National Research Fund (a member of Qatar Foundation). The statements made herein are solely the responsibility of the authors.

Nomenclature

r = radius (mm)
R_2 = impeller outer diameter
T = diffusion coefficient
$\mathbf{u}$ = flow velocity vector
$\mathbf{u}_g$ = mesh velocity of the moving mesh
U_2 = impeller tip speed (m/s)
ρ = fluid density (kg/m^3)
ϕ = the source term of ϕ

Abbreviations

CFD = computational fluid dynamics
LES = large eddy simulation
MBPF = main blade passing frequency
NASA = National Aeronautics and Space Administration
RMS = root mean square
SBPF = splitter blade passing frequency
URANS = unsteady Reynolds-averaged Navier–Stokes

References

[1] Borello, D., Hanjalic, K., and Rispoli, F., 2007, "Computation of Tip-Leakage Flow in a Linear Compressor Cascade With a Second-Moment Turbulence Closure," Int. J. Heat Fluid Flow, **28**(4), pp. 587–601.
[2] Denton, J. D., 1993, "The 1993 IGTI Scholar Lecture: Loss Mechanisms in Turbomachines," ASME J. Turbomach., **115**(4), pp. 621–656.
[3] McMullan, W. A., and Page, G. J., 2012, "Towards Large Eddy Simulation of Gas Turbine Compressors," Prog. Aerosp. Sci., **52**, pp. 30–47.
[4] Tauveron, N., 2010, "Simulation of a Compressor Cascade With Stalled Flow Using Large Eddy Simulation With Two-Layer Approximate Boundary Conditions," Nucl. Eng. Des., **240**(2), pp. 321–335.
[5] Tyacke, J., Tucker, P., Jefferson-Loveday, R., Vadlamani, N. R., Watson, R., Naqavi, I., and Yang, X., 2014, "Large Eddy Simulation for Turbines: Methodologies, Cost and Future Outlooks," ASME J. Turbomach., **136**(6), p. 061009.
[6] Gourdain, N., 2013, "Validation of Large-Eddy Simulation for the Prediction of Compressible Flow in an Axial Compressor Stage," ASME Paper No. GT2013-94550.
[7] Semlitsch, B., Jyothishkumar, V., Mihaescu, M., Fuchs, L., and Gutmark, E. J., 2013, "Investigation of the Surge Phenomena in a Centrifugal Compressor Using Large Eddy Simulation," ASME Paper No. IMECE2013-66301.
[8] Hellstrom, F., Gutmark, E., and Fuchs, L., 2012, "Large Eddy Simulation of the Unsteady Flow in a Radial Compressor Operating Near Surge," ASME J. Turbomach., **134**(5), p. 051006.
[9] McKain, T. F., and Holbrook, G. J., 1997, "Coordinates for a High Performance 4:1 Pressure Ratio Centrifugal Compressor," NASA Lewis Research Center, Cleveland, OH, Report No. NASA-23268.
[10] Spakovszky, Z. S., 2004, "Backward Traveling Rotating Stall Waves in Centrifugal Compressors," ASME J. Turbomach., **126**(1), pp. 1–12.
[11] Skoch, G. J., Prahst, P. S., Wernet, M. P., and Strazisar, A. J., 1997, "Laser Anemometer Measurements of the Flow Field in a 4:1 Pressure Ratio Centrifugal Impeller," ASME Paper No. 97-GT-342.
[12] Wernet, M. P., Bright, M. M., and Skoch, G. J., 2002, "An Investigation of Surge in a High-Speed Centrifugal Compressor Using Digital PIV," ASME J. Turbomach., **123**(2), pp. 418–428.
[13] Ni, R. H., and Fan, G., 2009, "CFD Simulation of a High-Speed Centrifugal Compressor Using Code Leo and Code Wand," AeroDynamic Solutions, Inc., Pleasanton, CA, Technical Report.
[14] Lurie, E. A., Vane Slooten, P. R., Medic, G., Mulugeta, J. M., Holley, B. M., Feng, J., Sharma, O., and Ni, R. H., 2011, "Design of a High Efficiency Compact Centrifugal Compressor for Rotorcraft Applications," The American Helicopter Society 67th Annual Forum, Virginia Beach, VA, May 3–5.
[15] Lim, K., Yoon, S., Goyne, C., Lin, Z., and Allaire, P., 2012, "Design and Characterization of a Centrifugal Compressor Surge Test Rig," Int. J. Rotating Mach., **2011**, p. 738275.
[16] Trébinjac, I., Bulot, N., and Buffaz, N., 2011, "Analysis of the Flow in a Transonic Centrifugal Compressor Stage From Choke to Surge," Proc. Inst. Mech. Eng., Part A, **225**(7), pp. 919–929.
[17] Babak, M., 2010, "CFD Analysis of a Surge Suppression Device for High Pressure Ratio Centrifugal Compressor," ANSYS Conference 2010, Frymburk, Czech Republic, Oct. 6–8.
[18] Galindo, J., Climent, H., Guardiola, C., and Tiseira, A., 2009, "On the Effect of Pulsating Flow on Surge Margin of Small Centrifugal Compressors for Automotive Engines," Exp. Therm. Fluid Sci., **33**(8), pp. 1163–1171.
[19] Bulot, N., Trébinjac, I., Ottavy, X., Kulisa, P., Halter, G., Paoletti, B., and Krikorian, P., 2009, "Experimental and Numerical Investigation of the Flow Field in a High-Pressure Centrifugal Compressor Impeller Near Surge," Proc. Inst. Mech. Eng., Part A, **223**(6), pp. 657–666.
[20] Bulot, N., and Trébinjac, I., 2009, "Effect of the Unsteadiness on the Diffuser Flow in a Transonic Centrifugal Compressor Stage," Int. J. Rotating Mach., **2009**, p. 932593.
[21] Arnulfi, G., Blanchini, F., Giannattasio, P., Micheli, D., and Pinamonti, P., 2005, "Extensive Study on the Control of Centrifugal Compressor Surge," Proc. Inst. Mech. Eng., Part A, **220**(3), pp. 289–304.
[22] Stein, A., 2000, "Computational Analysis of Stall and Separation Control in Centrifugal Compressors," Ph.D. thesis, Georgia Institute of Technology, Atlanta, GA.
[23] Ferrara, G., Ferrari, L., and Baldassarre, L., 2004, "Rotating Stall in Centrifugal Compressor Vaneless Diffuser: Experimental Analysis of Geometrical Parameters Influence on Phenomenon Evolution," Int. J. Rotating Mach., **10**(6), pp. 433–442.
[24] ANSYS, 2013, "ANSYS FLUENT Theory Guide" ANSYS Inc., Canonsburg, PA.
[25] Shahin, I., Gadala, M., Alqaradawi, M., and Badr, O., "Unsteady CFD Simulation for High Speed Centrifugal Compressor Operating Near Surge," ASME Paper No. GT2014-27336.
[26] Hathaway, M. D., Herrick, G., Chen, J., and Webster, R., 2004, "Time Accurate Unsteady Simulation of the Stall Inception Process in the Compression System of a US Army Helicopter Gas Turbine Engine," Users Group Conference (DOD_UGC'04), Williamsburg, VA, June 7–11, pp. 166–177.
[27] Crevel, F., Gourdain, N., and Moreau, S., 2014, "Numerical Simulation of Aerodynamic Instabilities in a Multistage High-Speed High-Pressure Compressor on Its Test-Rig—Part I: Rotating Stall," ASME J. Turbomach., **136**(10), p. 101003.
[28] Crevel, F., Gourdain, N., and Ottavy, X., 2014, "Numerical Simulation of Aerodynamic Instabilities in a Multistage High-Speed High-Pressure Compressor on Its Test Rig—Part II: Deep Surge," ASME J. Turbomach., **136**(10), p. 101004.